

Large and unsaturated negative magnetoresistance induced by the chiral anomaly in the Weyl semimetal TaP

Chandra Shekhar¹ *, Frank Arnold¹ *, Shu-Chun Wu¹, Yan Sun¹, Marcus Schmidt¹, Nitesh Kumar¹, Adolfo G. Grushin², Jens H. Bardarson², Ricardo Donizeth dos Reis¹, Marcel Naumann¹, Michael Baenitz¹, Horst Borrmann¹, Michael Nicklas¹, Elena Hassinger¹, Claudia Felser¹, & Binghai Yan^{1,2} †

¹Max Planck Institute for Chemical Physics of Solids, 01187 Dresden, Germany

²Max Planck Institute for the Physics of Complex Systems, 01187 Dresden, Germany

* These authors contributed equally to this work

The Weyl semimetal (WSM) is a topological quantum state ¹ wherein the bulk electronic bands disperse linearly along all momentum directions through a node, the Weyl point, in a 3D analogue of graphene. In momentum space, the Weyl point acts as a monopole with fixed chirality and promises the realization of an exotic quantum phenomenon: the chiral anomaly ^{2,3}. A fundamental consequence of the chiral anomaly is the non-conservation of the number of fermions with a given chirality when they are coupled to non-orthogonal electric (E) and magnetic (B) fields, and it is expected to induce unconventional negative magnetoresistance (MR) in WSMs ⁴. Therefore, the discovery of WSM materials ⁵⁻⁷ has recently stimulated an extensive experimental search for signatures of the chiral anomaly. Here, we report the observation of a large and unsaturated, negative MR induced by chiral anomaly in TaP, which was recently predicted to be a WSM ^{6,7}. We observe that the MR is negative

only when the magnetic field and the current are parallel within two degrees and is otherwise positive. The existence of a negative MR is independent of the current direction in the lattice as long as it is parallel to the magnetic field, and remains robust at temperatures below 20 K. With increasing field up to 14T, the MR decreases down to nearly -80% and exhibits no signature of saturation, which distinguishes TaP clearly from other WSMs such as TaAs^{8,9} reported recently. We use angle-resolved quantum oscillation spectra in combination with band-structure calculations to establish the Fermi surface topology in great detail, and find that Weyl points and Fermi pockets (both electron and hole) coexist at the Fermi energy. The anomalous negative MR due to chiral anomaly overwhelms the positive contribution of the trivial Fermi pockets in high fields, giving rise to the net negative MR observed. Our work demonstrates unsaturated chiral anomaly induced transport properties of WSM and thus promises exciting applications for valleytronics¹⁰⁻¹³ and spintronics¹⁴.

In a semimetal the conduction and valence bands may present an accidental touching at isolated points of the three-dimensional (3D) momentum (k) space, where the band disperses linearly from the touching point. Depending on whether bands are non-degenerate or doubly degenerate, such a 3D semimetal is called Weyl semimetal (WSM)^{1,15,16} or Dirac semimetal (DSM)¹⁷⁻¹⁹, respectively. Correspondingly, the band touching point is referred to as a Weyl point or a Dirac point. The Dirac point can split into two Weyl points either by breaking the crystal inversion symmetry or time-reversal symmetry (TRS). At energies close to Weyl points, electrons behave effectively as Weyl fermions, a fundamental kind of massless fermions that have never been observed as an elementary particle²⁰. In condensed-matter physics, each Weyl point act like a singularity of the

Berry curvature in the Brillouin zone (BZ), equivalent to magnetic monopoles in k -space, and thus they always occur in pairs with opposite chirality or handedness²¹. In the presence of nonorthogonal magnetic (\mathbf{B}) and electric (\mathbf{E}) fields (i.e. $\mathbf{E} \cdot \mathbf{B}$ is nonzero), the particle number for a given chirality is not conserved quantum mechanically, a phenomenon known as the Adler-Bell-Jackiw anomaly or chiral anomaly in high energy physics^{2,3,20}. The chiral anomaly can be simply understood by considering the zeroth Landau level (LLs) of a WSM in the quantum limit⁴. As illustrated in Fig. 1, the zeroth LL associated with the left-handed and right-handed Weyl node have opposite Fermi velocities, due to their different chirality. An applied electric field leads to an imbalance of electrons in the left-handed and right-handed valleys, breaking the number conservation of electrons for a given chirality. This effect, however, is not restricted to the quantum limit and recently it was proposed to induce an anomalous DC conductivity that depends quadratically on the magnetic field strength in the semi-classical limit²². The field enhanced conductance or, equivalently, a field reduced resistance – termed negative magnetoresistance (MR)⁴ – is a central feature originating from the chiral anomaly that can be detected in experiment; positive MR, which is insensitive to the field direction, is usually observed in normal semiconductors, semimetals and metals. The observation of the chiral anomaly induced MR requires that directions of the applied magnetic field and current should be as parallel as possible. Otherwise the negative MR will easily be overwhelmed by the positive contribution of the Lorentz force. Thus, the negative MR is anticipated to exist in a very narrow window of the angle between current and magnetic field²³. In ideal conditions the quadratic negative MR of a WSM is anticipated to dominate over all other contributions to MR^{32,33}. Further, a high quality of single crystal samples is necessary to fix the chemical potential

in the vicinity of Weyl points and also to minimize the impurity or defect scattering. In addition to a negative MR, the chiral anomaly also predicts an anomalous Hall effect^{16,24–26} and non-local transport properties^{13,27} to occur in WSMs.

The discovery of different WSM materials has stimulated recent efforts to experimentally confirm the chiral anomaly in condensed-matter physics. Very recently, the negative MR has been reported in two types of WSMs: DSMs with TRS breaking by external field, e.g. $\text{Bi}_{1-x}\text{Sb}_x$ ($x \approx 3\%$)²⁸, ZrTe_5 ²⁹ and Na_3Bi ²³, and inversion asymmetric WSMs TaAs^{8,9}, NbP³⁰ and NbAs³¹. However, the negative MR observed in these systems, except that of Na_3Bi , usually saturates at a small amplitude at low magnetic fields and ultimately becomes positive at high magnetic fields, which causes the signature of the chiral anomaly to be elusive³⁴. For example in TaAs, the MR goes through a minimum of -30% around 5 T and subsequently increases to positive values at high fields ($B \geq 9$ T) in Ref. 8, and MR remains positive in the whole field range measured in Ref. 9 for the same material. In addition, the existence of open Fermi surfaces at the boundary, dubbed Fermi arcs, is another important manifestation of the non-trivial topological nature of WSMs¹. These exotic surface states have been subject of intense angle-resolved photoemission spectroscopy (ARPES) studies in this WSM family such as TaAs^{35–37} and NbAs³⁸, and are also predicted to be sensitive to the chiral anomaly³⁹.

In this work, we report a large negative MR in the WSM material TaP. At low temperature, we observe a quadratic negative MR of about 80% up to the highest magnetic field (14 T) without any signs of saturation. The MR exhibits sensitive dependence on the angle (θ) between the magnetic

field and the current directions and becomes negative only for $\theta \leq 2^\circ$, which distinguishes it from the conventional magneto-transport. We observe negative MR when the current flows along the crystallographic a and c axes as long as $\mathbf{B} \parallel \mathbf{E}$, indicating robust chiral anomaly effect. The MR behavior remains essentially unaltered for $T < 20$ K. We reconstruct the 3D Fermi surfaces by combining the Shubnikov-de Haas (SdH) and de Haas-van Alphen (dHvA) oscillations and *ab initio* band structures. We reveal that the Fermi energy lies close to the Weyl points, confirming that negative MR indeed originates from the chiral anomaly in TaP.

We have synthesized high quality single crystals of TaP by the chemical vapor transport reactions and verified TaP as a non-centrosymmetric compound in a tetragonal lattice (space group $I4_1md$, No.109). The temperature-dependent resistivity exhibits typical semimetallic behavior. For more details please see in the Supplementary Information (SI).

We focus on the magneto-transport properties of TaP. From the same batch of samples, we set up two devices where current (\mathbf{I}) directions are along the crystallographic a (labeled S1) and c (label S2) axes, respectively. The angular dependence of the MR = $(R(\mathbf{B}) - R(0))/R(0)$ measured at 1.85 K are shown in Figs. 2A-B for both samples, where $R(\mathbf{B})$ is the resistance at the magnetic field \mathbf{B} . For $\theta = 90^\circ$ at $\mathbf{B} = 9$ T ($\perp \mathbf{I}$), the MR is as large as +15,000% and +18,000% for S1 and S2, respectively. On reducing θ , the MR drops quickly toward zero at a given magnetic field. At $\theta = 0^\circ$ ($\mathbf{B} \parallel \mathbf{I}$), the MR becomes negative for both samples. The MR is negative only in a very narrow window of $\theta \leq 2^\circ$ and becomes positive otherwise, as shown in the right panels of Figs. 2A-B. The small θ window of negative MR is similar to that observed in Na_3Bi ²³. Its independence

on the lattice direction (e.g. a or c axis) strongly supports the existence of the chiral anomaly.

Next, we concentrate on the $\mathbf{B}||\mathbf{I}$ case and increase the magnetic field up to 14 T to analyze the field and temperature dependence of the MR (see Figs. 2C-D). At 1.85 K, the MR first increases slightly and soon continues by a steep drop from positive to negative values. A similar positive MR region was also observed in $\text{Bi}_{1-x}\text{Sb}_x$ ²⁸, TaAs^{8,9} and other WSMs²⁹⁻³¹, attributed to an instead of the plausible weak anti-localization (WAL) effect. When $\mathbf{B} > 3.5$ T and $\mathbf{B} > 5.5$ T for S1 and S2, respectively, the total MR becomes negative. Up to the highest magnetic field applied (14 T), the MR decreases monotonically down to about -80% for S1 and -60% for S2 without signatures of saturation. This clearly distinguishes TaP from other WSMs. The MR curves remain almost unchanged in the temperature range of $T < 20$ K, indicating the robustness of the topological nature of the chiral magneto-transport. The MR increases for higher temperatures and turns fully positive for $T > 150$ K and 100 K in S1 and S2, respectively. The observable sinusoidal oscillations, superimposed onto the MR of S1 and S2 for $B > 10$ T, are SdH oscillations which attributed to conventional electron and hole pockets in TaP. These Fermi pockets allow for additional positive MR contributions from normal carriers to compete with the negative contribution from the chiral anomaly. Although the contribution due to the Lorentz force disappears for $\mathbf{B}||\mathbf{I}$, normal carriers can still exhibit a positive MR with $1/(1 + B^2)$ type field-dependence in the longitudinal conductivity (σ_{xx}) driven by the Fermi surface anisotropy⁴⁰. Simultaneously the chiral anomaly induces negative MR with B^2 type dependence in σ_{xx} ²². Therefore, normal positive MR prevails at low fields and anomalous negative MR can dominate at high fields, consistent with our

observations. This discussion motivates the use of a simple formula to fit σ_{xx} ,

$$\sigma_{xx} = \frac{\sigma_1}{1 + a_1 B^2} + \frac{\sigma_2}{1 + a_2 B^2} + cB^2 \quad (1)$$

where the last term is the chiral anomaly part with coefficient c , the first two terms are normal carrier contributions, $\sigma_{1,2}$ are zero field conductivities and $a_{1,2}$ are corresponding coefficients of field dependence. We note that two $1/(1 + B^2)$ terms are indeed necessary to obtain a satisfactory fitting, and SdH oscillations are neglected. As will be clear from the fermiology analysis, highly anisotropic electron and hole pockets coexist at the Fermi energy, which justifies the introduction of the first two terms in Eq. 1. The accurate fitting results for the MR at 1.85 K (fitting for all temperature range can be found in SI), shown in the insets of Figs. 2E-F, support our simple competition scenario of the MR. As the temperature increases, the chiral anomaly coefficient c is found to drop quickly and become almost zero after 150 K for S1 and S2. For $T \leq 20$ K, the slight deviation from quadratic dependence in high field ($B > 10$ T) probably indicates that the system is approaching quantum limit, where σ_{xx} due to the chiral anomaly should be linear in B ^{4,41}. This interpretation is consistent with the Fermi pocket sizes that we obtain from our fermiology analysis below.

We extract the carrier information from the temperature dependent Hall measurement in the $\mathbf{B} \perp \mathbf{I}$ case. At low temperature, the negative slope in high fields represents the electron dominated transport (also see SI). As temperature increases, the negative slope turns to be positive with the transition temperature being around 150 K. The sign change of the Hall resistivity indicates that the semimetal is close to the electron-hole compensation point, which is also similar to the Hall effect observed in TaAs^{8,9} and NbP^{14,30}. We employ a two-carrier model (see Ref. 42) to fit the Hall

conductivity (σ_{xy}) and longitudinal conductivity σ_{xx} , and extract the mobility and concentration of electrons and holes for the device S1 (similar results obtained also for S2, see SI). As shown in Fig. 3A, we find that at 1.85 K the concentration of electrons ($n_e \approx 1.2 \times 10^{19} \text{ cm}^{-3}$) is slightly higher than that of holes ($n_h \approx 0.6 \times 10^{19} \text{ cm}^{-3}$), while the mobility of electrons ($\mu_e \approx 2 \times 10^4 \text{ cm}^2/Vs$) is lower than that of holes ($\mu_h \approx 9 \times 10^4 \text{ cm}^2/Vs$). The experimental error bars are around 30% for both the carrier concentration and mobility. High mobility values indicate the high quality of the single crystals where the impurities and defects are expected to be very few. From the above carrier concentrations one can deduce that the fully compensated situation is reached when $n_e = n_h \approx 0.9 \times 10^{19} \text{ cm}^{-3}$. These values are of the same order of magnitude as the theoretical values $n_e = n_h = 1.8 \times 10^{19} \text{ cm}^{-3}$, according to the volumes of electron and hole pockets in our density-functional theory (DFT) calculations. Based on the values of n_e and n_h in the Hall measurement, we deduce that the Fermi energy of the sample is approximately 5 meV above the compensation point, where $n_e = 2.2 \times 10^{19} \text{ cm}^{-3}$ and $n_h = 1.4 \times 10^{18} \text{ cm}^{-3}$ in theory.

The fermiology of TaP is investigated by means of quantum oscillations. Typically, for a semimetal with light carriers and high mobility as for example bismuth⁴³, prominent oscillations appear in all measurable properties sensitive to the density of states at the Fermi energy. Here, we have measured SdH oscillations in transport (Figure 2A-F) and dHvA oscillations in magnetization (Fig. 3B) and torque. These oscillations are periodic in $1/B$ and their frequency (F) is proportional to the extremal Fermi surface cross section (A_k) that is perpendicular to \mathbf{B} following the Onsager relation $F = (\Phi_0/2\pi^2)A_k$, where $\Phi_0 = h/2e$ is the magnetic flux quantum and h is the Planck constant. Figure 3B shows the magnetic dHvA oscillations as a function of the inverse field (inset)

and their corresponding Fourier transform (main panel) for $\mathbf{B}||c$. Here the observable fundamental frequencies are $F_\alpha = 15$ T, $F_\beta = 18$ T and $F_\delta = 45$ T. The frequencies are consistent for all three measurement techniques and different samples batches. This shows that all samples share the same chemical potential and the resistivity measurements are sensitive to the bulk Fermi surface as well. For $\mathbf{B}||a$ the main frequencies are $F_\gamma = 34$ T, $F_{\gamma''} = 95$ T and $F_{\delta'} = 160$ T, clearly indicating anisotropic 3D Fermi surface pockets. For most of the detected oscillation frequencies we derive their cyclotron effective masses (m^*) of the carriers by fitting the temperature dependence of the oscillation amplitude with the Lifshitz-Kosevich formula (see Ref. 44 and SI). The values of the effective masses are $m_\alpha^* = 0.02 m_0$, $m_\beta^* = 0.04 m_0$ and $m_\delta^* = 0.11 m_0$ for $\mathbf{B}||c$ whereas they are 4-10 times higher for $\mathbf{B}||a$ with $m_\gamma^* = 0.16 m_0$, $m_{\gamma''}^* = 0.34 m_0$ and $m_{\delta'}^* = 0.4 m_0$ in this case, where m_0 is the mass of a free electron (see table I in SI). These values are very low and comparable to the effective masses in other slightly doped Dirac materials such as Cd_3As_2 or graphene^{45,46}.

To reconstruct the exact shape of the Fermi surface, the full angular dependence of the quantum oscillation frequencies is measured and compared to band structure calculations (Fig. 3C). The exact position of the Fermi energy (E_F) is determined by matching the calculated frequencies and their angular dependence to the measured ones (see SI for more details). The best fit is obtained when E_F lies 5 meV above the ideal electron-hole compensation point in agreement with the resulting carrier concentration from the Hall measurements. Calculations reveal two banana-shaped Fermi surface pockets at such E_F , a hole banana (H) and a slightly larger electron banana (E). These two pockets well reproduce the angular dependence of measured dHvA frequencies with great accuracy (see lines in Fig. 3C and the 3D Fermi surface in Fig. 4). E - and H -bananas are

almost semi circular and distribute along the predicted nodal rings from band-crossing lines^{6,6,7} in the BZ. The rather isotropic frequencies F_α and F_γ result from a neck and extra humps at the end of the hole banana (see Figure 4B). Extra splittings of some frequencies with field angles departing from $\mathbf{B}||c$ are explained by the existence of four bananas in the BZ each turned by 90° for both E and H pockets. Additionally, in dHvA experiment the mobility of the hole orbits (F_α, F_β) was extracted via the width of the Fourier transform peaks which is given by the exponential decrease of the oscillations with $1/B$ (the so-called Dingle term, see SI). The mobility is $\mu_h = 3.2 \times 10^4$ ($\pm 20\%$) cm^2/Vs , which is of the same order of magnitude as found from the Hall effect.

The measured Fermi surface topology and carrier concentration described above converge to the same statement that the Fermi energy (E_F) of our samples is 5 meV above the ideal charge-neutral point in the calculated band structure. The consistency between experiment and theory strongly suggests that this is the true Fermi surface of our TaP samples. We plot the corresponding 3D Fermi surfaces from the *ab initio* calculations in Fig. 4. One can see that E - and H -pockets are the only two pockets at the Fermi energy.

Next, we investigate the Weyl points in the band structure. In the 3D BZ, there are twelve pairs of Weyl points with opposite parity: four pairs lie in the $k_z = 0$ plane, labelled as W1; eight pairs stay in planes close to $k_z = \pm\pi/c$ (c is the lattice constant), labelled as W2. One can find that W1 points are far below E_F by 47 meV and are included in the E -pocket. Here the energy barrier between a pair of W1 points totally disappears (Fig. 4C), so that W1-type Weyl points cannot give rise to a detectable chiral anomaly effect in TaP. The W2-type Weyl points are, on the other hand,

14 meV above E_F and separated by a 16 meV barrier along the line connecting the Weyl point pair with opposite chirality. Such pairs of W2 points merge slightly into the head position of the H -pocket, leading to a two-horn-like cross-section (see F_γ in Fig. 4B). We plot the energy dispersion of Weyl bands over the F_γ plane in Fig. 4D. The Weyl cone is strongly anisotropic in the lower cone region below the Weyl point, where there is a very small energy barrier of $1\sim 2$ meV between two Weyl points along a winding k -path. Despite the existence of the low-barrier winding pathway, we argue that W2 points can still behave as independent Weyl fermions in a magnetic field along a generic direction (e.g. along a or c axis). In our band structure calculations, we find very similar anisotropic W2 Weyl cones all four WSMs of this family: TaAs, TaP, NbAs and NbP. Similar to our present analysis of TaP, the lower W2 Weyl cones were also speculated to account for the chiral anomaly induced negative MR in TaAs^{8,9}, although detailed fermiology measurement was lacking. The effect of anisotropic Weyl nodes, as well as the small energy barrier between left and right movers, can be modeled theoretically with an extension of the Weyl theory that includes coupling at higher energies of the two chiralities (see Ref. 26). Although these two effects will typically compete with the chiral $\mathbf{E} \cdot \mathbf{B}$ contribution, they are not expected to annihilate the effect as long as the Fermi energy is lower than the energy barrier separating the two species (the W2 case in Fig. 4C). On the other hand, provided that the highly anisotropic E - and H -pockets are not in the quantum limit, they are expected to contribute only a positive MR rather than a negative MR at $\mathbf{B} \parallel \mathbf{I}$ ⁴⁰. Indeed, recalling that all quantum oscillation frequencies are larger than 15 T, the E - and H -pockets do not enter the quantum limit when negative MR starts to appear at $B \sim 5$ T, which excludes another trivial origin of negative MR³⁴. In addition, it is inconsistent to assume the

Fermi energy to cross the W1 Weyl points; otherwise we should observe a hole-dominated carrier concentration with negligible electrons, which is in conflict with our experimental data. Therefore, we can attribute the negative MR observed to the chiral anomaly related to the W2-type of Weyl points.

In summary, we observe a large negative magnetoresistance caused by the chiral anomaly in the inversion-asymmetric WSM TaP. Such negative MR exists only when the magnetic field is parallel to the current with less than two degrees angle variation, but is insensitive to the direction of the current with respect to the lattice, which distinguishes it clearly from conventional magneto-transport. Accurate angle-dependent Fermi surface measurements (SdH and dHvA) and band structure calculations reveal the coexistence of banana-shaped anisotropic electron and hole pockets, which give rise to normal positive MR that dominates only at small fields. Our experimental data combined with the theoretical analysis shows that the W2-type Weyl valleys lie near the Fermi energy and induce the chiral transport effect for the negative MR that overwhelms conventional transport. The large unsaturated negative MR that we find as a function of magnetic field opens the way towards using a fundamental quantum phenomena, the chiral anomaly, as a building block for novel devices.

Methods *Single crystal growth.* High-quality single crystals of TaP were grown via a chemical vapor transport reaction using iodine as a transport agent. Initially, polycrystalline powder of TaP was synthesized by a direct reaction of tantalum (Chempur 99.9%) and red phosphorus (Heraeus 99.999%) kept in an evacuated fused silica tube for 48 hours at 800 °C. Starting from this micro-

crystalline powder, the single-crystals of TaP were synthesized by chemical vapor transport in a temperature gradient starting from 850 °C (source) to 950 °C (sink) and a transport agent with a concentration of 13,5 mg/cm³ iodine (Alfa Aesar 99,998%)⁴⁷. The orientation and crystal structure of the present single crystals were investigated using the diffraction data sets collected on a Rigaku AFC7 diffractometer equipped with a Saturn 724+ CCD detector (monochromatic MoK_α radiation, $\lambda = 0.71073$ Å). Structure refinement was performed by full-matrix least-squares on F^2 within the program package WinCSD.

Magnetoresistance measurement. The resistivity measurements were performed in physical property measurement systems (PPMS, Quantum Design, DC resistivity in AC option). From the Laue diffraction, we selected two different orientated the crystals. They have been named as S1 and S2, and their detail analysis of orientations is given in SI part of manuscript. The physical dimensions of the crystals are $0.42 \times 0.16 \times 1.1$ mm³ for S1 and $0.48 \times 0.27 \times 0.8$ mm³ for S2. All the contacts on the crystals were made by Pt wire with 25 micrometer diameter using spot welding. These crystals have been mounted on PPMS rotational puck in such way that current can be passed along the length i.e. current along a -axis for S1 and c -axis for S2. Four probes normal resistivity and Hall resistivity have been measured by passing a current of 3 milliamperes at temperatures range 1.85 – 300 K and field ± 14 T. To find the negative magnetoresistance, we have taken an extra attention in current and field directions during mounting the crystals in rotational puck. We obtained almost symmetrical resistivity signal in positive and negative field directions otherwise transverse resistivity and Hall signals overwhelm the negative MR. The angular dependencies of the resistance were measured using the PPMS rotator option. For resistivity and general

characterization measurements the build-in PPMS AC-Transport option was used, whilst highly sensitive Shubnikov-de Haas measurements used external Stanford Research SR830 lock-in amplifiers. Here typical excitation currents of a few milliampere were applied at frequencies of about 20 Hz. The Hall contributions to the longitudinal resistance and vice versa due to contact misalignment were accounted for by calculating the mean or differential resistance of positive and negative magnetic fields.

Magnetization. The magnetism and magnetic quantum oscillations of TaP along the main crystallographic axes were measured in a Quantum Design SQUID-VSM. The angular dependencies were measured using the Quantum Design piezo-resistive torque magnetometer (Tq-Mag⁴⁸) in a PPMS with installed rotator option. Magnetization and torque measurements were performed on two large 4.4 and 21.7 mg TaP single crystals. The samples were mounted on the sample holder and torque lever by GE varnish or Apiezon N grease and aligned along their visible crystal facets, which was confirmed by X-ray diffraction measurements. The crystal alignment was verified by photometric methods and showed typical misalignments of less than 2°. SQUID magnetization measurements were performed for static positive and negative magnetic fields up to 7 T in the temperature range of 2 to 50 K. Magnetic torque measurements were performed up to 14 T in the same temperature range. Here the sample is mounted on a flexible lever which bends when torque is applied. The sample magnetization M induces a magnetic torque $\tau = M \times B$, which bends the lever and can be sensed by piezo-resistive elements which are micro-fabricated onto the torque lever. These elements change their resistance under strain and are thus capable of sensing the bending of the torque lever. The unstrained resistance of these piezo-resistors is typically 500

Ω and can change by up to a few percent when large magnetic torques are applied. Measuring quantum oscillations, however, requires a higher torque resolution. Thus the standard torque option was altered and extended by an external balancing circuit and SR830 lock-in amplifiers as read-out electronic. This way a resolution of one in 10^7 was achieved. The magnetic torque was measured for magnetic fields in the (100), (001) and (110)-plane in angular steps of 2.5° and 5° . Measurements were taken during magnetic field down sweeps from 14 to 0 T. The magnetic field sweep rate was adjusted such that the sweep rate in $1/B$ was constant. The resultant magnetic torque signals are a superposition of the sample diamagnetism, de Haas-van Alphen oscillation and uncompensated magneto-resistance of the piezo-resistors. Due to the vector product of the magnetization and magnetic field, this method can only be applied to samples with strong Fermi surface anisotropy and is insensitive when the magnetic field and magnetization are aligned parallel, e.g. along the crystallographic c -direction in TaP. The quantum oscillation frequencies are extracted from the measured resistivities and magnetizations by subtracting all back ground contributions to those signals and performing a Fourier transformation of the residual signal over the inverse magnetic field. The resulting spectra show the de Haas-van Alphen frequencies and their amplitude.

Band structure calculations. The *ab initio* calculations were performed using density-functional theory with the Vienna *ab-initio* simulation package⁴⁹. Projector-augmented-wave potential represented core electrons. The modified Becke-Johnson exchange potential^{50,51} was employed for accurate band structure calculations. Fermi surfaces were interpolated using maximally localized Wannier functions (MLWFs)⁵² in dense k -grids (equivalent to $300 \times 300 \times 300$ in the whole BZ).

Then angle-dependent extremal cross-sections of Fermi surfaces are calculated to compare with the transport oscillation frequencies according to the Onsager relation.

Acknowledgements We are grateful for L.-K. Lim, E. G. Mele, Z.-K. Liu and Y.-L. Chen for helpful discussions. This work was financially supported by the Deutsche Forschungsgemeinschaft DFG (Project No. EB 518/1-1 of DFG-SPP 1666 "Topological Insulators") and by the ERC Advanced Grant No. (291472) "Idea Heusler".

Competing Interests The authors declare that they have no competing financial interests.

Correspondence Correspondence and requests for materials should be addressed to B. Yan (email: yan@cpfs.mpg.de).

1. Wan, X. G., Turner, A. M., Vishwanath, A. & Savrasov, S. Y. Topological semimetal and Fermi-arc surface states in the electronic structure of pyrochlore iridates. *Phys. Rev. B* **83**, 205101 (2011).
2. Adler, S. L. Axial-Vector Vertex in Spinor Electrodynamics. *Phys. Rev.* **177**, 2426–2438 (1969).
3. Bell, J. S. & Jackiw, R. A PCAC puzzle: $\pi^0 \rightarrow \gamma\gamma$ in the σ -model. *Nuov Cim A* **60**, 47–61 (1969).
4. Nielsen, H. B. & Ninomiya, M. The Adler-Bell-Jackiw anomaly and Weyl fermions in a crystal. *Phys. Lett. B* **130**, 389–396 (1983).

5. Liu, Z. K. *et al.* Discovery of a Three-Dimensional Topological Dirac Semimetal, Na₃Bi. *Science* **343**, 864–867 (2014).
6. Weng, H., Fang, C., Fang, Z., Bernevig, B. A. & Dai, X. Weyl Semimetal Phase in Noncentrosymmetric Transition-Metal Monophosphides. *Phys. Rev. X* **5**, 011029 (2015).
7. Huang, S.-M. *et al.* An inversion breaking Weyl semimetal state in the TaAs material class. *arXiv* (2015). 1501.00755.
8. Huang, X. *et al.* Observation of the chiral anomaly induced negative magneto-resistance in 3D Weyl semi-metal TaAs. *arXiv* (2015). 1503.01304.
9. Zhang, C. *et al.* Observation of the Adler-Bell-Jackiw chiral anomaly in a Weyl semimetal. *arXiv* (2015). 1503.02630.
10. Turner, A. M. & Vishwanath, A. Beyond Band Insulators: Topology of Semi-metals and Interacting Phases. *arXiv* (2013). 1301.0330.
11. Hosur, P. & Qi, X. L. Recent developments in transport phenomena in Weyl semimetals. *Comptes Rendus Physique* **14**, 857–870 (2013).
12. Vafeek, O. & Vishwanath, A. Dirac Fermions in Solids: From High-T cCuprates and Graphene to Topological Insulators and Weyl Semimetals. *Ann. Rev. Cond. Matter Phys.* **5**, 83–112 (2014).

13. Parameswaran, S. A., Grover, T., Abanin, D. A., Pesin, D. A. & Vishwanath, A. Probing the chiral anomaly with nonlocal transport in three-dimensional topological semimetals. *Phys. Rev. X* **4**, 031035 (2014).
14. Shekhar, C. *et al.* Extremely large magnetoresistance and ultrahigh mobility in the topological Weyl semimetal NbP. *arXiv* (2015). 1502.04361.
15. Volovik, G. Quantum analogues: From phase transitions to black holes and cosmology. *eds. William G. Unruh and Ralf Schutzhold, Springer Lecture Notes in Physics* **718**, 31–73 (2007).
16. Burkov, A. A. & Balents, L. Weyl Semimetal in a Topological Insulator Multilayer. *Phys. Rev. Lett.* **107**, 127205 (2011).
17. Murakami, S. Phase transition between the quantum spin Hall and insulator phases in 3D: emergence of a topological gapless phase. *New J. Phys.* **10**, 029802 (2008).
18. Young, S. M. *et al.* Dirac Semimetal in Three Dimensions. *Phys. Rev. Lett.* **108** (2012).
19. Fang, C., Gilbert, M. J., Dai, X. & Bernevig, B. A. Multi-Weyl Topological Semimetals Stabilized by Point Group Symmetry. *Phys. Rev. Lett.* **108** (2012).
20. Bertlmann, R. A. *Anomalies in quantum field theory*, vol. 91 (Oxford University Press, 2000).
21. Nielsen, H. B. & Ninomiya, M. Absence of neutrinos on a lattice. *Nuclear Physics B* **185**, 20–40 (1981).
22. Son, D. T. & Spivak, B. Z. Chiral anomaly and classical negative magnetoresistance of Weyl metals. *Phys. Rev. B* **88**, 104412 (2013).

23. Xiong, J. *et al.* Signature of the chiral anomaly in a Dirac semimetal: a current plume steered by a magnetic field. *arXiv* (2015). 1503.08179.
24. Xu, G., Weng, H., Wang, Z., Dai, X. & Fang, Z. Chern Semimetal and the Quantized Anomalous Hall Effect in HgCr_2Se_4 . *Phys. Rev. Lett.* **107** (2011).
25. Yang, K.-Y., Lu, Y.-M. & Ran, Y. Quantum Hall effects in a Weyl semimetal: Possible application in pyrochlore iridates. *Phys. Rev. B* **84**, 075129 (2011).
26. Grushin, A. G. Consequences of a condensed matter realization of Lorentz-violating QED in Weyl semi-metals. *Phys. Rev. D* **86** (2012).
27. Zhang, C. *et al.* Detection of chiral anomaly and valley transport in Dirac semimetals. *arXiv* (2015). 1504.07698v1.
28. Kim, H.-J. *et al.* Dirac versus weyl fermions in topological insulators: Adler-bell-jackiw anomaly in transport phenomena. *Phys. Rev. Lett.* **111**, 246603 (2013).
29. Li, Q. *et al.* Observation of the chiral magnetic effect in ZrTe_5 . *arXiv* (2014). 1412.6543.
30. Wang, Z. *et al.* Helicity protected ultrahigh mobility Weyl fermions in NbP. *arXiv* (2015). 1506.00924v2.
31. Yang, X., Liu, Y., Wang, Z., Zheng, Y. & Xu, Z.-A. Chiral anomaly induced negative magnetoresistance in topological Weyl semimetal NbAs. *arXiv* (2015). 1506.03190.
32. Burkov, A. A. Chiral Anomaly and Diffusive Magnetotransport in Weyl Metals. *Phys. Rev. Lett.* **113**, 247203 (2014).

33. Burkov, A. A. Negative longitudinal magnetoresistance in Dirac and Weyl metals. *arXiv* (2015). 1505.01849v1.
34. Goswami, P., Pixley, J. H. & Das Sarma, S. Axial anomaly and longitudinal magnetoresistance of a generic three dimensional metal. *arXiv* (2015). 1503.02069v1.
35. Xu, S.-Y. *et al.* Experimental realization of a Weyl semimetal phase with Fermi arc surface states in TaAs. *arXiv* (2015). 1502.03807.
36. Lv, B. Q. *et al.* Discovery of Weyl semimetal TaAs. *arXiv* (2015). 1502.04684.
37. Lv, B. Q. *et al.* Observation of Weyl nodes in TaAs. *arXiv* (2015). 1503.09188.
38. Xu, S.-Y. *et al.* Discovery of Weyl semimetal NbAs. *arXiv* (2015). 1504.01350.
39. Behrends, J., Grushin, A. G., Ojanen, T. & Bardarson, J. H. Visualizing the chiral anomaly in Dirac and Weyl semimetals with photoemission spectroscopy. *arXiv* (2015). 1503.04329.
40. Pal, H. K. & Maslov, D. L. Necessary and sufficient condition for longitudinal magnetoresistance. *Phys. Rev. B* **81**, 214438 (2010).
41. Aji, V. Adler-Bell-Jackiw anomaly in Weyl semimetals: Application to pyrochlore iridates. *Phys. Rev. B* **85** (2012).
42. Takahashi, H., Okazaki, R., Yasui, Y. & Terasaki, I. Low-temperature magnetotransport of the narrow-gap semiconductor FeSb_2 . *Phys. Rev. B* **84**, 205215 (2011).
43. Edel'Man, V. Electrons in bismuth. *Advances in Physics* **25**, 555–613 (1976).

44. Shoenberg, D. *Magnetic oscillations in metals* (Cambridge University Press, 1984).
45. Rosenman, I. Effet shubnikov de haas dans Cd_3As_2 : Forme de la surface de fermi et modele non parabolique de la bande de conduction. *J. Phys. Chem. Solid* **30**, 1385–1402 (1969).
46. Novoselov, K. *et al.* Two-dimensional gas of massless dirac fermions in graphene. *nature* **438**, 197–200 (2005).
47. Martin, J. & Gruehn, R. Zum Chemischen Transport von Monophosphiden MP (M= Zr, Hf, Nb, Ta, Mo, W) und Diphosphiden MP₂ (M= Ti, Zr, Hf). *Z. Kristallogr* **182**, 180 (1988).
48. Rossel, C. *et al.* Active microlevers as miniature torque magnetometers. *J. Appl. Phys.* **79**, 8166–8173 (1996).
49. Kresse, G. & Furthmüller, J. Efficient iterative schemes for ab initio total-energy calculations using a plane-wave basis set. *Phys. Rev. B* **54**, 11169 (1996).
50. Becke, A. D. & Johnson, E. R. A simple effective potential for exchange. *J. Chem. Phys.* **124**, 221101 (2006).
51. Tran, F. & Blaha, P. Accurate band gaps of semiconductors and insulators with a semilocal exchange-correlation potential. *Phys. Rev. Lett.* **102**, 226401 (2009).
52. Mostofi, A. A. *et al.* wannier90: A tool for obtaining maximally-localised Wannier functions. *Compu. Phys. Commun* **178**, 685–699 (2008).

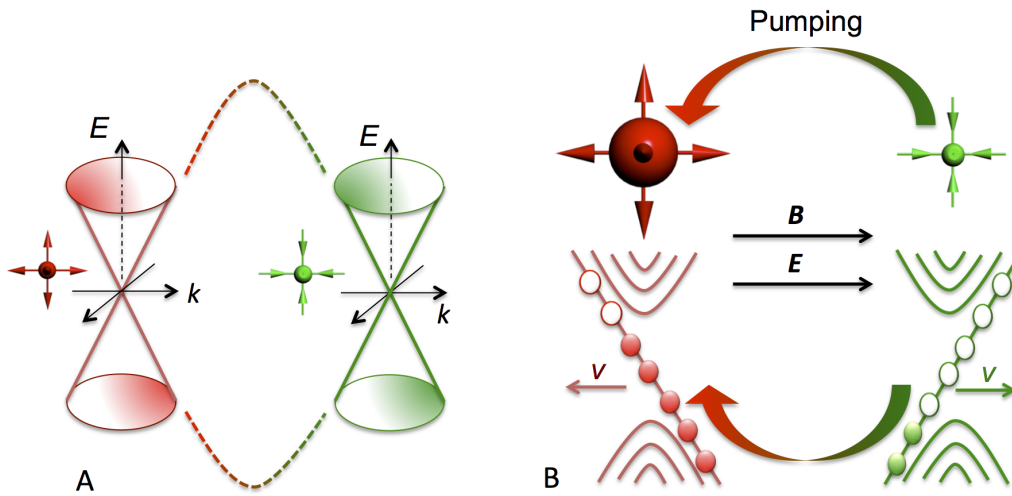


Figure 1 Illustration of Weyl points with opposite chirality and chiral anomaly. **A**, A pair of Weyl points with left-handed (left) and right-handed (right) chirality. Arrows stand for the Berry curvature or Chern flux. **B**, Charge pumping between two Weyl points when $\mathbf{B} \parallel \mathbf{E}$. Left- and right-handed Weyl nodes exhibit opposite velocity (v) in the zeroth Landau level (lower panel). Then electric field induces the increase and decrease of electron numbers in the left- and right-hand nodes (upper panel), respectively, leading to the chiral anomaly effect.

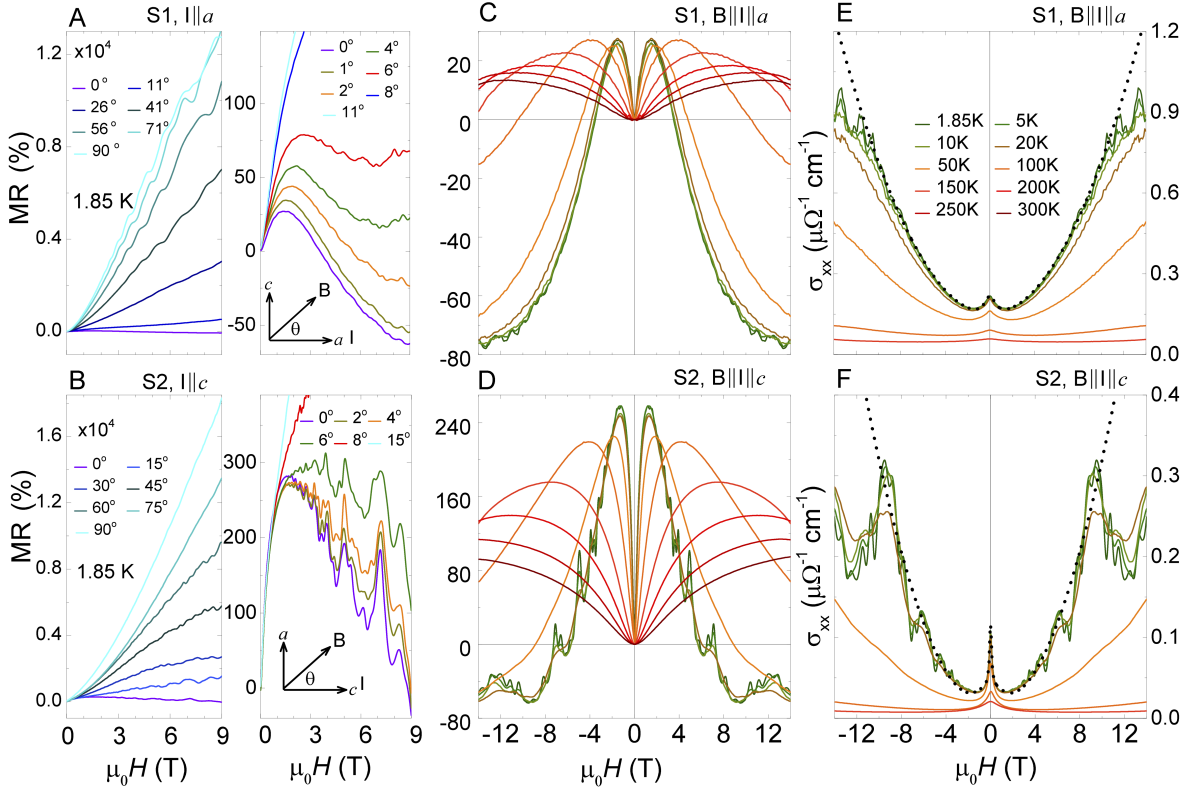


Figure 2 Negative magnetoresistance (MR) due to chiral anomaly. Upper and lower panels correspond to the results measured on device S1 ($I||a$) and S2 ($I||c$), respectively. **A**, **B**, MR dependence on the angle (θ) between magnetic field and current. The right panel is a zoom-in of the small θ region. **C**, **D**, Negative MR at different temperature. The MR at $\theta = 0^\circ$ in B and D are slightly different, which is due to the modification of the current contact, but both present the negative MR. **E**, **F**, Conductivity (σ_{xx}) corresponding to C and D, respectively. Solid-curves with different colors represent temperature from 1.85 K to 300 K, as labelled in E. The dotted curves represent fitting of σ_{xx} at 1.85 K according to Eq. 1.

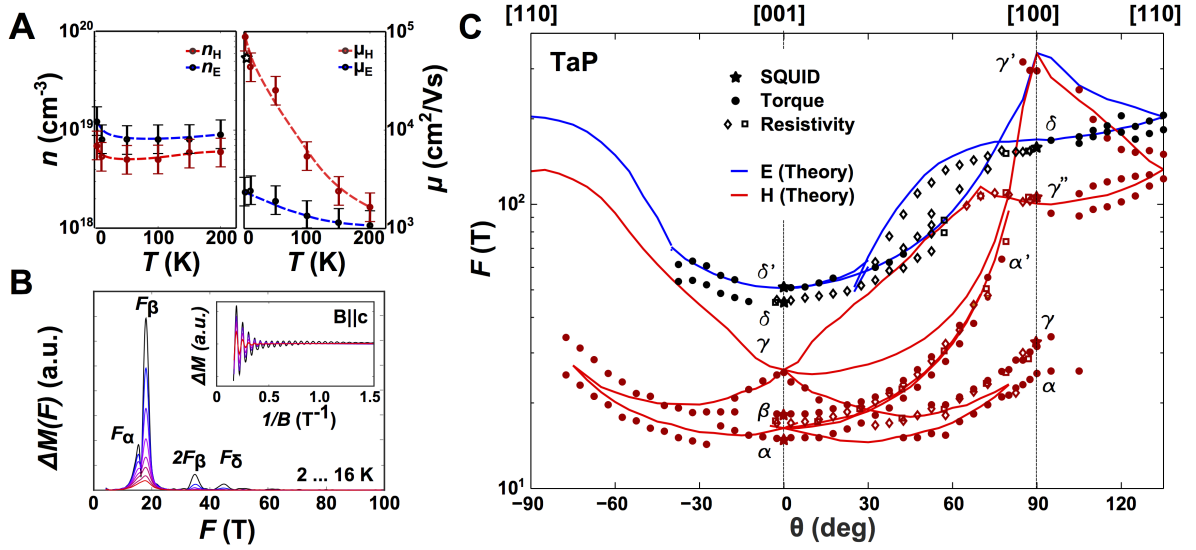


Figure 3 Carrier concentrations and quantum oscillations in TaP. **A**, Carrier concentration and mobility of the hole (H) and electron (E) pockets obtained by fitting the temperature-dependent Hall resistivity in device S1. The mobility of the hole labeled by a star is determined from dHvA analysis. **B**, Quantum oscillations in the magnetization (inset) for $\mathbf{B}||c$ and their Fourier transform spectrum. **C**, The full angular dependence of the measured oscillation frequencies (different symbols for different measurement methods on crystals from two batches) and the calculated frequencies by DFT from the 3D Fermi surface (solid lines) shown in Fig. 4.

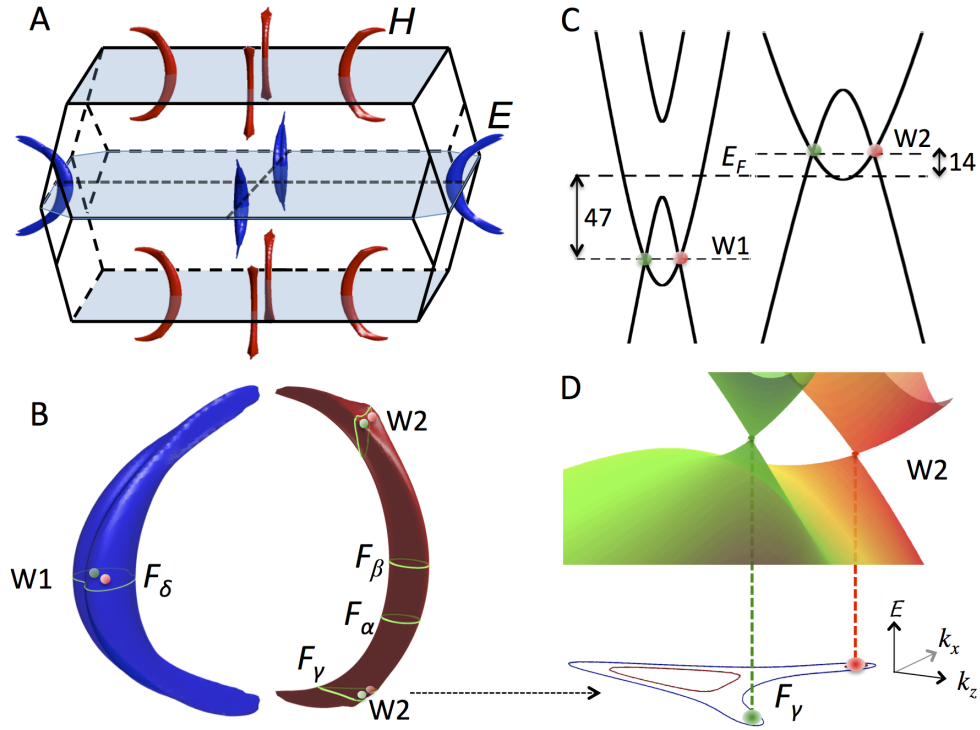


Figure 4 3D Fermi pockets and Weyl points. **A**, Fermi pockets in the first Brillouin zone at the Fermi energy (E_F) detected in the experiment. The electron (E) and hole (H) pockets are represented by blue and red color, respectively. **B**, Zoom-in of the E - and H -pockets of banana shape. The pink and green points indicate the Weyl points with opposite chirality. $W1$ - and $W2$ -type of Weyl points can be found inside E - and close to H -pockets, respectively. Green loops show some extremal cross-sections of E and H , corresponding to the oscillation frequencies measured $F_{\alpha,\beta,\gamma,\delta}$ (see the text). **C**, The energy dispersion

along the connecting line between a pair of Weyl points with opposite chirality for W1 (left) and W2 (right). The deduced experimental E_F (thick dashed horizontal line) is 14 meV below W2 and 47 meV above W1 Weyl points. **D**, Strongly anisotropic Weyl cones originating from a pair of W2-type Weyl points on the plane of F_γ . Green and red Weyl cones represent the opposite chirality.